



HAL
open science

Dawn-dusk asymmetry in the main auroral emissions at Jupiter observed with Juno-UVS

A. Groulard, B. Bonfond, D. Grodent, J. -C. Gérard, T. K. Greathouse, V. Hue, G. R. Gladstone, M. H. Versteeg

► **To cite this version:**

A. Groulard, B. Bonfond, D. Grodent, J. -C. Gérard, T. K. Greathouse, et al.. Dawn-dusk asymmetry in the main auroral emissions at Jupiter observed with Juno-UVS. *Icarus*, 2024, 413, <10.1016/j.icarus.2024.116005>. <insu-04726503>

HAL Id: insu-04726503

<https://insu.hal.science/insu-04726503v1>

Submitted on 26 Mar 2025

HAL is a multi-disciplinary open access archive for the deposit and dissemination of scientific research documents, whether they are published or not. The documents may come from teaching and research institutions in France or abroad, or from public or private research centers.

L'archive ouverte pluridisciplinaire **HAL**, est destinée au dépôt et à la diffusion de documents scientifiques de niveau recherche, publiés ou non, émanant des établissements d'enseignement et de recherche français ou étrangers, des laboratoires publics ou privés.



Distributed under a Creative Commons CC BY 4.0 - Attribution - International License

1 Dawn-dusk asymmetry in the main auroral emissions at Jupiter 2 observed with Juno-UVS

3

4 A. Groulard¹, B. Bonfond^{1*}, D. Grodent¹, J.-C. Gérard¹, T. K. Greathouse², V. Hue³, G. R.
5 Gladstone², M. H. Versteeg²

6 *Corresponding author: b.bonfond@uliege.be

7 ¹Laboratory for Planetary and Atmospheric Physics, Space Sciences, Technologies and
8 Astrophysical Research Institute, University of Liège, Liège, Belgium

9 ²Southwest Research Institute, San Antonio, TX, USA

10 ³Aix-Marseille Université, CNRS, CNES, Institut Origines, LAM, Marseille, France

11

12 **0 | Abstract**

13

14 Jupiter's main auroral emissions usually form auroral curtains surrounding the magnetic
15 poles. Most explanations for this auroral feature are based on corotation enforcement
16 currents flowing between the magnetosphere and the ionosphere. This process predicts the
17 highest emitted power to originate from the dawn region, while the lowest emitted power
18 would come from the noon to dusk region. However, a previous study using Hubble Space
19 Telescope data showed the opposite, with a higher emitted power in the dusk region in the
20 south and ambiguous results in the north. In the present study, we use data from the first
21 39 Juno perijoves to reexamine this question. We find a dusk region 3.3 to 5.5 times more
22 powerful than the dawn one, in qualitative agreement with the previous study but contrary
23 to theoretical expectations. These results support the idea that the main emissions cannot
24 be fully described by corotation enforcement currents.

25

26 **1| Introduction**

27

28 The UV aurorae at Jupiter are made of various structures having different origins (see e.g.
29 the review in Grodent, 2015). The main emissions are the most easily identifiable of them.
30 They generally take the shape of an almost closed curtain centered on the jovimagnetic
31 poles (the intersections of the magnetic dipole axis with the surface), with a systematic
32 brightness decrease between 10:00 and 12:00 magnetic local time (Radioti et al., 2008). In
33 the southern hemisphere, the nearly dipolar field gives an oval shape to the main emissions,
34 while a magnetic anomaly related to the high order terms of the magnetic field multipolar
35 development gives them a bean shape in the northern hemisphere (Grodent et al., 2008;
36 Connerney et al., 2022). The persistence of this main component of the aurorae is
37 presumably due to its formation mechanism.

38

39 The most widely accepted explanation for the main auroral emissions at Jupiter before the
40 Juno era was related to the magnetosphere-ionosphere coupling current system enforcing
41 the partial corotation of the plasma in the Jovian middle magnetosphere (Cowley and
42 Bunce, 2001; Hill, 2001). When particles produced by the volcanically active moon Io are
43 ionized, they end up forming a plasma torus around Jupiter, corotating with the planet
44 along the moon's orbit. Because of a balance between centrifugal, thermal and Lorentz
45 forces, the plasma in the torus progressively diffuses radially outward into a plasmashet. A
46 corotation enforcement current loop arises to maintain the corotation of the plasma,
47 transferring angular momentum from Jupiter's polar atmosphere to the magnetosphere. In
48 the equatorial plane of the magnetosphere, this current flows radially, which manifests as

49 an azimuthal bendback of the magnetic field lines. It then flows along magnetic field lines
50 and closes in the ionosphere via Pedersen currents. As the iogenic plasma moves further
51 away from the planet, the upward (relative to Jupiter) field aligned currents (FACs) enforce a
52 significant degree of corotation ($\sim 75\text{-}90\%$ of full corotation) up to around $20\text{-}40 R_J$ before
53 the plasma's angular velocity starts to drop significantly at larger distances. The field aligned
54 currents peak in this transition region where the corotation breaks down. According to this
55 family of models, such upward FACs accelerate electrons towards Jupiter's atmosphere via
56 quasi-static electric fields, generating the main auroral emissions at the feet of the field
57 lines. The main emissions magnetically map to distances between 15 and 60 Jupiter radii (R_J)
58 in the magnetosphere (Vogt et al., 2011), similarly to estimated magnetospheric roots of the
59 field aligned current sheets observed by Juno (Kamran et al., 2022). This theory provides a
60 straightforward explanation for the persistence of the main emissions over long timescales
61 and for the existence of the field aligned currents inferred from magnetic field
62 measurements (Kamran et al., 2022; Kotsiaros et al., 2019; Nichols and Cowley, 2022;
63 Sulaiman et al., 2022). However, Bonfond et al., (2020) have questioned this simplified
64 picture recently after highlighting an increasing number of observations which appear in
65 contradiction with the model's expectations. For example, as the magnetic field topology
66 and plasma flow are not uniform around the planet, Ray et al. (2014) used a 1-D model
67 based on this theory to predict how the intensity of the main emission varies over local
68 times. According to this model, the strongest aurorae should take place at dawn and should
69 be at least one order of magnitude stronger than in the dusk region. . This prediction has
70 been tested by Bonfond et al. (2015) , who used Hubble Space Telescope (HST) data to
71 determine and compare the power emitted in the dusk and dawn parts of the main
72 emissions. They found a dusk region about 3 times more powerful than the dawn one in the

73 southern hemisphere, which is in disagreement with the Ray et al. (2014) model. They also
74 have found that both regions were equally powerful in the northern hemisphere. However,
75 they noted that the later results should be considered with caution. Indeed, the HST
76 observations are hampered by the telescope's viewing geometry, which is such that HST
77 cannot observe the night side aurora and most images are acquired when the jovimagnetic
78 pole of interest is tilted towards the Earth. This issue is more prominent in the north since
79 the barycenter of the main auroral emission is located at lower latitude. This limitation is
80 further magnified by the presence of a large magnetic anomaly near 100° System III
81 longitude. System III is the longitude system fixed with Jupiter's magnetic field extensively
82 used to study the magnetic phenomena taking place at Jupiter. Based on their results in the
83 southern hemisphere, which they considered more reliable, the authors concluded that the
84 main emissions cannot be fully described by the theory of partial corotation enforcement in
85 the middle magnetosphere. The partial ring current observed at Jupiter (Khurana, 2001) has
86 been suggested to generate FACs increasing the emitted power in the dusk region, and
87 lowering it in the dawn region, to explain the disagreement between their results and the
88 model. The purpose of the present study is to further constrain the findings of Bonfond et
89 al. (2015) with observations unaffected by Earth orbit viewing geometry.

90

91 The morphology and intensity of the main emissions may also vary over a few hours. For
92 example, instead of a simple and well defined arc, the main emissions sometimes appear to
93 form forks and parallel arcs, and patchy features can be seen from time to time (Nichols et
94 al., 2009). In addition to these disturbances, two kinds of events can increase the emitted
95 power of the aurorae (Yao et al., 2022): dawn storms and main auroral brightenings.

96 Bonfond et al. (2021) have found dawn storms in about half of the first 20 Juno perijoves
97 (PJ). They also extended the definition of these storms to a chain of events lasting from 5 to
98 10 hours, ending with 1 to 2 hours of intense brightening of the dawn region of the main
99 emissions. A more global brightening coupled with a shrinking of the main emission can also
100 occur during solar wind compressions of the magnetosphere (Nichols et al., 2007, 2009,
101 2017; Yao et al., 2022).

102 The discrepancy between the dawn/dusk auroral power ratio in the northern and southern
103 hemispheres based on the HST data called for a re-investigation of this problem with
104 unbiased data. Here we carry out a similar study, based on UV auroral observations carried
105 out with the Ultraviolet Spectrograph on board the Juno spacecraft.

106

107 **2| Observations**

108

109 The NASA Juno spacecraft arrived at Jupiter on July 5th, 2016 (Bolton et al., 2017). It was
110 placed in a highly eccentric polar orbit bringing it to an altitude of only 4000 km at its
111 periapsis, and out to 8 million km near apoapsis well out into the magnetosphere. This orbit
112 offers the advantage of gathering high resolution data of Jupiter, while being able to study
113 the whole environment of the planet. Juno is a spinning spacecraft, undergoing one rotation
114 every 30 s. It carries 10 scientific instruments, including a longslit UltraViolet Spectrograph
115 (UVS) used in this study. UVS is a photon-counting imaging spectrograph operating in the
116 68-210 nm range (Gladstone et al., 2017). The UVS field of view consists of a 7.2° long slit
117 divided into three parts. The 2 external parts are 0.2° wide, while the central one is

118 narrower and has a width of only 0.025° . Individual photons are counted and calibrated
119 using the effective area derived from many stellar observations (Hue et al., 2019), while the
120 wavelength registration comes from pre-launch measurements (Davis et al., 2011; Hue et
121 al., 2021). As they provide a higher signal-to-noise ratio, only the external wider parts of the
122 slit were used in this study. The data used for this study are selected among the
123 observations acquired with Juno-UVS during four hours in each hemisphere when the
124 spacecraft flies over the poles close to its perijove.

125

126 We first created polar brightness maps of the aurorae in the same way as described by
127 Bonfond et al. (2021). Specifically, after removing the noise from the images, data gathered
128 over 100 spins of the spacecraft were added and weighted to build the final map. This
129 method has the advantage of allowing the creation of comprehensive maps of the aurorae
130 for most of the perijoves, but the tradeoff is a long (~ 50 minutes) time interval between the
131 first and the last spins. This process was repeated for the first 39 perijoves of Juno in both
132 hemispheres. Because of the limited coverage of the poles by Juno during some perijoves,
133 only 63 maps were considered in the study. More precisely, out of the 39 possible maps for
134 each perijove, 38 were kept in the southern hemisphere and 25 in the northern hemisphere.
135 The detailed times of observation for each perijove can be found in the supplementary
136 material. In this study, we only considered the time intervals during which the high voltage
137 was nominal. The indicated brightness is the total FUV brightness emitted by H_2 in kR units.
138 In order to mitigate the effect of hydrocarbon absorption (especially methane, below 140
139 nm), we first only considered the unabsorbed 145-165 nm wavelength range and then
140 multiplied it by a factor of 4.4 to extend the brightness to the whole FUV H_2 spectrum. To

141 account for the fact that the assumed emitting surface is not perpendicular to the viewing
142 axis, we multiplied the observed brightness by the cosine of the local emission angle, which
143 typically lies around $\sim 30\text{-}40^\circ$. To derive the emitted power, we multiply the brightness by
144 the mean photon energy (1.65×10^{-18} J) and by the emission surface in the region of interest.

145

146 **3 | Analysis**

147

148 While the main emissions clearly stand out when co-adding many UV auroral images,
149 identifying them on individual images can become tricky when the morphology becomes
150 complex (parallel arc, dawn storms, etc.). In order to get robust results, we decided to use 3
151 different methods to build masks isolating the main emissions and we used 2 different
152 definitions of the dawn and dusk sectors. First, since the size of the main auroral oval varies
153 with time, we used a pair of “generic” masks, one for a contracted auroral oval and one for
154 an expanded auroral oval, using the one most appropriate for the case under study. This
155 method is somewhat similar to the one used by Bonfond et al. (2015), who used monthly
156 averaged reference ovals to build masks and then used this mask for all images during that
157 month. Then we built “adjusted” masks, fitting the location of the main emissions as closely
158 as possible for each individual image, but with a constant width. We then built masks by
159 fitting both the location and the width.

160

161 **3.1 | Main emissions masks**

162

163 The first mask built to isolate the main emissions, the Magnetospheric Distance mask (MD
164 mask), was created based on the Vogt et al. (2011) magnetic mapping model. It is thought to
165 be more reliable than models based on the combination of an internal field and a current
166 disk in the middle magnetosphere, which is the region where the plasma that feeds the
167 main emissions is located. Indeed, it accounts for the influence of local time on the
168 magnetic field and it is rooted on measurements of the Ganymede footprint path from the
169 Hubble Space Telescope and of magnetic flux in the equatorial plane from Galileo. Using this
170 model, two masks were created to cover locations mapping to a constant distance of 30 and
171 40 R_J in the magnetosphere to take into account the variable location of the main emissions.
172 Indeed, as already mentioned, Vogt et al. (2011) have found the main emission to map
173 between 15 and 60 R_J in the magnetosphere. We chose distances of 30 and 40 R_J as it is in
174 the middle of this interval so that we have better chances of covering the main emissions
175 well. To do so, we chose 36 equally spaced local times. Those are used to find the longitude
176 and latitude of the ionospheric locations mapping to these local times at a distance of 30
177 and 40 R_J in the magnetosphere based on the Vogt et al. (2011) model. These ionospheric
178 locations have then been interpolated to obtain ribbons covering all longitudes. At each
179 point constituting the ribbons, the widths of the ribbons have then been extended to 2° in
180 the direction of the axis linking that point to the barycenter of the aurorae, so that the
181 masks overlap most of the main auroral emissions without including contributions from
182 other auroral features. As the main emissions morphology changes over time, the location
183 of its barycenter can also slightly move. Still, in this study we assumed the barycenter to be
184 located at 73.9° latitude and 185.6° System III longitude in the north; and -81.9° latitude and
185 31.9° System III longitude in the south since its exact location does not have a marked
186 impact on our results. These locations have been derived from images coming from the

187 2007 HST campaign. To choose between the contracted oval mask and the expanded oval
188 mask, we computed the total power in the area covered by both masks. The mask with the
189 largest total power was kept as the MD mask (Figure 1, panel 2a), while the other one was
190 discarded. In order to be able to select sub-elements of this mask corresponding to the
191 different local time sectors, our masks are not just binary masks, but each element of the
192 mask is attributed a value related to the angle centered on the barycenter of the aurorae
193 (Figure 1, panel 2b).

194

195 The two other masks were created based on the actual location of the MEs in the images.
196 Because arcs can be present not only in the MEs, but also on the polar region and in the
197 equatorward emissions, we must exclude these regions from our search and focus on the
198 region where they are the most likely to appear. To do so, we decided to use as a first guess
199 the suite of masks based on the 2007 HST campaign (Bonfond et al., 2012; Clarke et al.,
200 2009)The HST mask with the best overlap of the main emission was chosen as a starting
201 point. For each tenth of a degree of longitude, the brightness peak was searched in the
202 surrounding of the HST mask, assuming this peak is due to the main emissions. The HST
203 mask has essentially been used to restrict the search area and make sure to discard the IFP
204 which can be brighter than the main emissions in some locations. For areas where the main
205 emissions are fainter than usual, the highest gradient of brightness was searched instead of
206 the highest brightness. Indeed, based on the idea that the main emissions are associated
207 with FACs due to corotation enforcement, they should correspond to an auroral curtain with
208 a higher peak brightness than its surrounding, and a high gradient of brightness should be
209 present at its edges. Once done for all the longitudes of interest, a Fourier series was fitted

210 to the locations thus found. This method results in a smooth ribbon at the center of the
211 main emissions. As for the MD mask, the ribbon was extended to be 2° wide to cover the
212 whole width of the main emissions. An example of such an AF1 mask over the aurorae can
213 be seen in Figure 1, panel 3a. The mask also has different values for different angles around
214 the barycenter of the aurorae for later considerations (Figure 1, panel 3b).

215

216 The last mask is the Auroral Fit with variable width mask (AF2 mask). It has been created to
217 take into account the complex shape that the main emissions can take during some
218 perijoves. When the main emissions are composed of parallel arcs or unusual particularly
219 wide features, it can be more extended than 2°. Thus, the two first masks may be too
220 narrow in several places, and a third one is needed to more accurately deal with these
221 unusual cases. To create the AF2 mask, we started from the boundaries of the AF1 mask. To
222 find broad auroral main emissions, we looked for high brightness regions partly covered by
223 the AF1 mask. To do so, we used a brightness threshold defined based on the brightness of
224 the area covered by the AF1 mask for each tenth of degree around the barycenter. If there
225 are emissions above that threshold just outside the AF1 mask, they are considered as part of
226 the main emissions and they must be covered by the mask. In this case, new limits are
227 defined to encompass them. If there is no such bright region, the AF1 limits are kept. After
228 that, the new inner and outer limits have been fitted independently with Fourier series, so
229 that it gives two ribbons that serve as the limits of the AF2 mask. This way, the mask is at
230 least 2° wide in latitude, but can be broader if the main emissions are more extended at
231 some locations (Figure 1, panel 4a). As for the two other masks, the value of the different
232 points of the mask is linked to its angle around the barycenter of the aurorae (Figure 1,

233 panel 4b). This mask is a generalized version of the AF1 mask. It has been needed for 27 of
234 the 63 maps, since its usefulness relies on an unusual shape of the main emissions. Out of
235 them, 8 are in the northern hemisphere, and 19 in the southern one. Even for these maps,
236 the broadening of the mask is not necessarily in the dusk or dawn region, and the AF2 mask
237 only has an impact on few perijoves.

238

239 **3.2| Dawn and dusk regions selection**

240

241 Two different local time extents of the dusk and dawn regions in the magnetosphere were
242 selected to study the emitted power. The first one, the B15 sector, ranges from 16:00 to
243 18:00 LT in the dusk region, and from 06:00 to 08:00 LT in the dawn region. Its size was set
244 to match the study performed by Bonfond et al. (2015) in order to compare our results to
245 theirs. The second one, the SYM sector, ranges from 16:00 LT to 20:00 LT in the dusk region,
246 and from 04:00 LT to 08:00 LT in the dawn one. This sector is symmetrical over the dusk
247 local time (i.e.: 18:00 LT) and the dawn local time (i.e.: 06:00 LT), which is a more natural
248 choice to study these regions. This sector could not be studied with HST due to its orbit that
249 did not allow for a view of the night part of the planet.

250

251 We used the Vogt et al. (2011) magnetic mapping model, with the JRM09 model
252 (Connerney et al., 2018) as input magnetic field model, to link the desired local times in the
253 magnetosphere to locations in the ionosphere. Each magnetospheric local time corresponds
254 to a given angle relative to the barycenter of the aurorae in the ionosphere. The model

255 provides a longitude-latitude location in the ionosphere from a location with a known
256 longitude and distance in the magnetosphere. The desired local times are used as the input
257 longitude, and a distance of $30 R_J$ is used as the input distance since it is expected to map to
258 the main emissions. All the ionospheric longitude-latitude coordinates can then be
259 transformed into polar coordinates. Thanks to the way the three masks were created, with
260 the value of a location proportional to its angle around the barycenter (Figures 1, panels b),
261 one can easily find the different sectors in the ionosphere from the locations expressed in
262 polar coordinates. This way, we have limited the main emissions masks to the two sectors of
263 interest to study the emitted power from the two regions.

264 The maps that could not be used at all because the aurorae were not well imaged have
265 already been ruled out of the study, but additional problems arise. Some UVS auroral maps
266 are incomplete in a part of the dusk or dawn region, and the main emissions mask is not
267 accurately placed in others. The second case mostly happens for the MD mask, which maps
268 to a constant distance in the magnetosphere, while the origin of the main emissions is at a
269 variable distance (see the example of PJ12 north in the supplemental material). Bonfond et
270 al. (2015) had already noted that in some rare cases, their generic monthly oval would
271 completely miss the aurora on one side (generally the dusk one). Because these cases are
272 both rare and lead to obviously erroneous results, the study has been restricted to 338
273 sectors out of the 378 possible sectors of the 63 maps.

274

275 **4| Results and discussion**

276

277 For each sector, the dusk-over-dawn power ratio was computed, and the results can be
278 seen in Figure 2. In the dataset of UVS auroral images analyzed here, the dusk sector is
279 brighter than the dawn sector in ~85% of the cases. Regardless of the size of the sector, the
280 reference oval in use and the assumed auroral width, the median power ratios are several
281 times larger than unity, indicating a dusk region more powerful than the dawn one (Table 1).
282 We note that, compared to a “generic mask” such as our MS mask, adjusting for the precise
283 location of the main emissions (AF1 masks), and to their width (AF2 masks) tends to
284 increase the value of the median ratio. This is because the adjusted masks better select the
285 more variable dusk arc (or multiple arcs). Furthermore, we note that, while the AF2 masks,
286 being wider, may capture emissions arising from different mechanisms than the rest of the
287 MEs, the inclusion of a larger region does not fundamentally modify the results.

288 In the B15 sector, the median ratio varies from 3.4 (MD mask) to 3.9 (AF2 mask) in the
289 northern hemisphere, while in the southern hemisphere it varies from 4.2 (MD mask) to 5.5
290 (AF2 mask). Thus, our results are qualitatively similar to those obtained by Bonfond et al.,
291 2015 in the south (a median dusk/dawn ratio of 3.1).. Additionally, our values in the north
292 are relatively similar to those in the south (3.4 compared to 4.2 for the B15 sector and the
293 MD mask, which the combination closest to the method used in Bonfond et al. 2015). This
294 result validates the reservations of Bonfond et al. (2015) concerning their own results in
295 north, which they considered unreliable because they were tainted by a selection bias.
296 Nevertheless, we note that our value in the south remains higher than the one deduced
297 from the HST images. We attribute at least part of the difference in the results to the color
298 ratio (CR) assumed to be constant over the main emissions in the previous study. The color
299 ratio measures the absorption of light from the atmospheric constituents and is given by the
300 ratio of intensity of light in an unabsorbed band (155-162 nm) and the intensity in an

301 absorbed band (123-130 nm) (Yung et al., 1982; Gustin et al., 2012). By assuming a constant
302 CR, they considered all the emissions to take place at the same depth. Gérard et al. (2016)
303 have shown that the brightness and the color ratio are correlated in the main emissions. The
304 throughput of the broadband filter used for Far-UV imaging with the Space Telescope
305 Imaging Spectrograph (STIS) and the Advanced Camera for Surveys (ACS) have a triangular
306 shape (see Figure1 in Gustin et al. 2012), putting an emphasis on the shorter wavelengths
307 (those absorbed by methane) Hence, for a similar initial brightness, the more absorbed
308 emissions appear attenuated in the images. As a consequence, when the color ratio and
309 brightness are correlated, the apparent contrast between bright and absorbed features on
310 one hand and dim but less absorbed features on the other hand is reduced. Because the
311 Juno-UVS observations provide spectral information between 68-210 nm, it is possible to
312 multiply the observed spectra by the throughput of the filters used by the cameras on board
313 HST to simulate these observations. A test applied to the southern hemisphere during PJ4
314 indeed showed that the use of the throughput of the HST SrF2 filter led to a ~10% decrease
315 on the dusk/dawn ratio, compared to the unaltered UVS brightness. However, this
316 computation assumes that HST can observe the Jovian pole from the same vantage point as
317 Juno. Changing the elevation angle from ~30° to ~80° would further increase the CR contrast
318 and thus decrease the dusk/dawn ratio.

319

320 Slightly lower dusk-over-dawn ratios are found in the SYM sector, with median ratios on the
321 order of 2.9 to 4.0. We attribute this to the size of the sectors. Indeed, the SYM sector is
322 twice larger than the B15. Thus, there are more chances for a bright patch of emission to be
323 covered by a given mask in the SYM sector. If this patch is in the dusk region, it has a low

324 impact on the ratio since the dusk region is generally made of bright emissions. Conversely,
325 if the patch is in the dawn region, it can have a larger impact, which results in lowering the
326 power ratio. Either way, we found a brighter dusk region for both sectors.

327 We computed the mean value and the variance of the emitted power in the different
328 sectors (table S4) and we did not find that the variance is significant different in one sector
329 compared to the other. Thus, the variability of the ratio cannot be preferentially attributed
330 to one local time sector. The power difference between the dusk and dawn sectors could
331 have been used as an alternative parameter (see its median values in table S3), but it would
332 lead to the same general conclusion, with the drawback of being sensitive to the size of the
333 sectors.

334

335 Some perijoves displayed a more powerful dawn region. This is the case for PJ3, 10, 12, 15,
336 18, 26 and 32. Different reasons can explain this trend. First, we have found dawn storms
337 during PJ3 and PJ32. These are not the only perijoves during which dawn storms have been
338 observed, but the others are captured at stages where the power amplification is not yet
339 present or significant enough to inverse the ratio. During PJ10, 12, 15 and 18, a main aurora
340 brightening (MAB) and a compression of the main emissions are visible. This case is often
341 coupled with a more complex morphology of the main emissions in the dusk region. Such
342 auroral morphologies are generally associated with the arrival of a solar wind shock
343 (Grodent et al., 2018; Nichols et al., 2007; Yao et al., 2022). Therefore, the MD and AF1
344 masks cannot cover the whole main emissions, and the dawn region seems more powerful
345 with these masks. When using the AF2 mask, the dusk region can be better covered, and the
346 power ratio goes back to a value closer to unity. No trend can be identified concerning the

347 more powerful region in this case, as the ratios have values slightly higher or lower than
348 unity. In the case of PJ26, the main emissions vanished in the dusk region of the northern
349 hemisphere, which led to the dawn section being brighter than the dusk one. The three
350 explanations for these low ratios are illustrated in Figure 3.

351

352 **5 | Summary and conclusion**

353

354

355 Using data gathered over the first 39 Juno perijoves, we have conducted a study of the
356 emitted power from the dusk and dawn regions of the main emissions. To analyze the
357 impact of the accuracy of the identification of the main emissions on the results, 3 different
358 masks have been created to isolate the regions. The first one uses the Vogt et al. (2011)
359 model to link the magnetospheric plasma to auroral features in order to build a “generic”
360 mask. The second one is built specifically for each image and covers the region of highest
361 brightness, assuming it is the main emissions. Finally, the third one is similar to the second
362 one, but with a variable width permitted to cover the wider parts of the main emissions. In
363 addition to these 3 masks, 2 sectors have been chosen for the study. The first sector extends
364 from 16:00 to 18:00 LT in the dusk region, and from 06:00 to 08:00 LT in the dawn one,
365 allowing for comparisons with previous results from Bonfond et al. (2015). The second
366 sector range chosen is an extension of the first one to set it symmetrically with respect to
367 the 18:00 LT and 06:00 LT directions, i.e., 16:00 to 20:00 LT in the dusk region, and 04:00 to

368 08:00 LT in the dawn region. Our analyses show that, whatever the combination of mask
369 and sector, we obtain the same results:

370

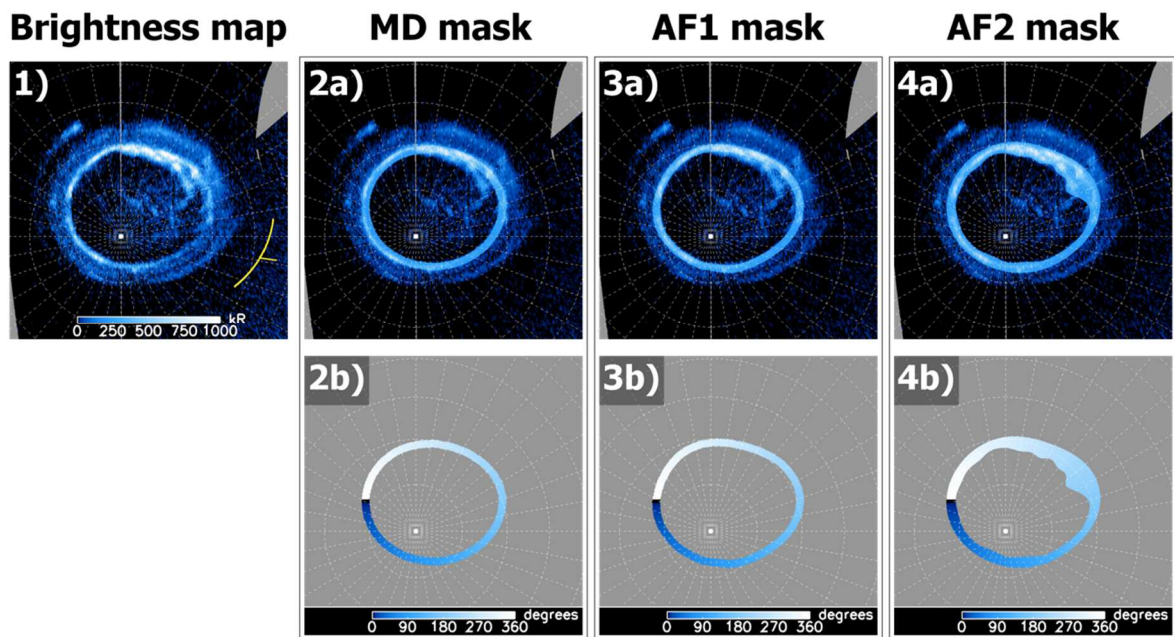
- 371 • The median dusk-over-dawn power ratios are ~3-4 times higher than unity for every
372 hemisphere, mask and sector, indicative of a dusk region generally more powerful.
373 We note that this behavior is seen whether the dusk-side main emissions are formed
374 of a single regular arc (e.g. PJ8 south) or display a more complex morphology.
- 375 • Some perijoves displayed a dawn region more powerful than the dusk one, and 3
376 main reasons can be evoked to explain it. There have been dawn storms during some
377 perijoves, main auroral brightenings due to increases in the solar wind ram pressure
378 in some others, and a surprising disappearance of the main emissions in the dusk
379 region has been found in the northern hemisphere of PJ26.

380

381 Our results are similar to those obtained by Bonfond et al. (2015) in the southern
382 hemisphere and are still opposite to the expectations from the modeling of (Ray et al.,
383 2014). The former suggested that, if the main emissions brightness is proportional to the
384 field aligned currents in the middle magnetosphere, then this asymmetry could be
385 qualitatively compatible with the combination of the upward (relative to the ionosphere)
386 FACs related to the corotation breakdown in the middle magnetosphere and the FACs
387 closing the partial ring currents in the ionosphere flowing downward in the dawn sector and
388 upward in the dusk sector (aka. Region 2 currents). Lorch et al. (2020) used data gathered
389 over 39 years with 7 spacecraft to study the asymmetry in the magnetodisk currents. They
390 found that azimuthal currents are fed at dusk and removed at dawn, in agreement with the

391 concept of partial ring current, confirming earlier results from Khurana (2001). On the other
392 hand, they also showed that the radial currents were weaker on the dusk side compared to
393 the dawn side beyond 30R_J. Thus, because they arise from the combination of these
394 opposite effects, the inferred total field aligned currents do not bear a clear and
395 unambiguous imprint of region 2 currents able to explain the auroral observations discussed
396 here. (Nichols and Cowley, 2022) showed an excellent temporal correlation between the
397 radial currents and the auroral brightness of the MEs on the dawn side. They also concluded
398 that the FACs related to the closure of the partial ring current in the dawn sector should be
399 ~10 times smaller than those associated with the drop of corotation in the middle
400 magnetosphere (0.25 $\mu\text{A}/\text{m}^2$ compared to 1-3 $\mu\text{A}/\text{m}^2$) and thus have a limited influence on
401 the aurora. Since the dusk side has the weakest radial currents but the brightest auroral
402 emissions, we must conclude that, despite the good temporal correlation observed on the
403 dawn side, there is no spatial correlation between the aurora and the radial currents.
404 Furthermore, if the closing of the partial ring current does not trigger a large auroral
405 response, then the auroral emissions do not provide a faithful image of the field aligned
406 currents, even in the MEs region. An alternative or supplemental explanation for the main
407 emissions could arise from the finding of stronger plasma turbulences on the dusk side of
408 the magnetosphere below 50 R_J compared to the dawn side (Tao et al., 2015). Indeed, other
409 aurora triggering processes involving ultra-low frequency (ULF) waves and/or Alfvén waves
410 have been discussed (Nichols et al., 2017b; Saur et al., 2018; Pan et al., 2021; Lorch et al.,
411 2022; Feng et al., 2022) and their impact on the brightness and morphology of the UV
412 auroral emissions would certainly deserve a closer exploration in a near future as the
413 evolution of Juno's orbit now allows dawn/dusk comparisons.

414

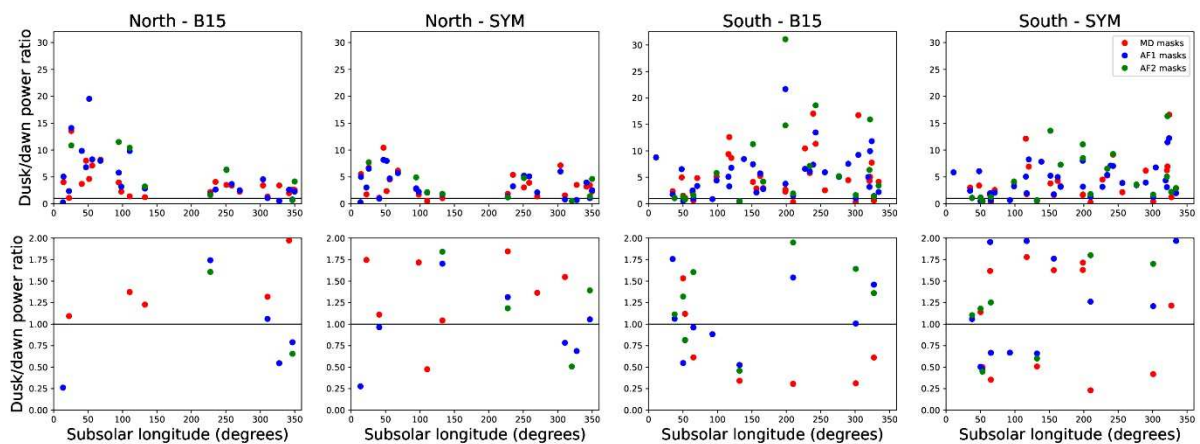


416

417 Figure 1: 1) Polar projection of the southern pole during PJ38. The sunward directions spanned over
 418 the data used to create the map are indicated by a yellow region, with the radially extended part
 419 referring to the mean sunward direction that has been used for the computations. For panels 2, 3
 420 and 4, images a) are the same polar projection as panel 1 with MD, AF1 and AF2 masks respectively
 421 added on. Images b) are polar projections of the masks alone.

422

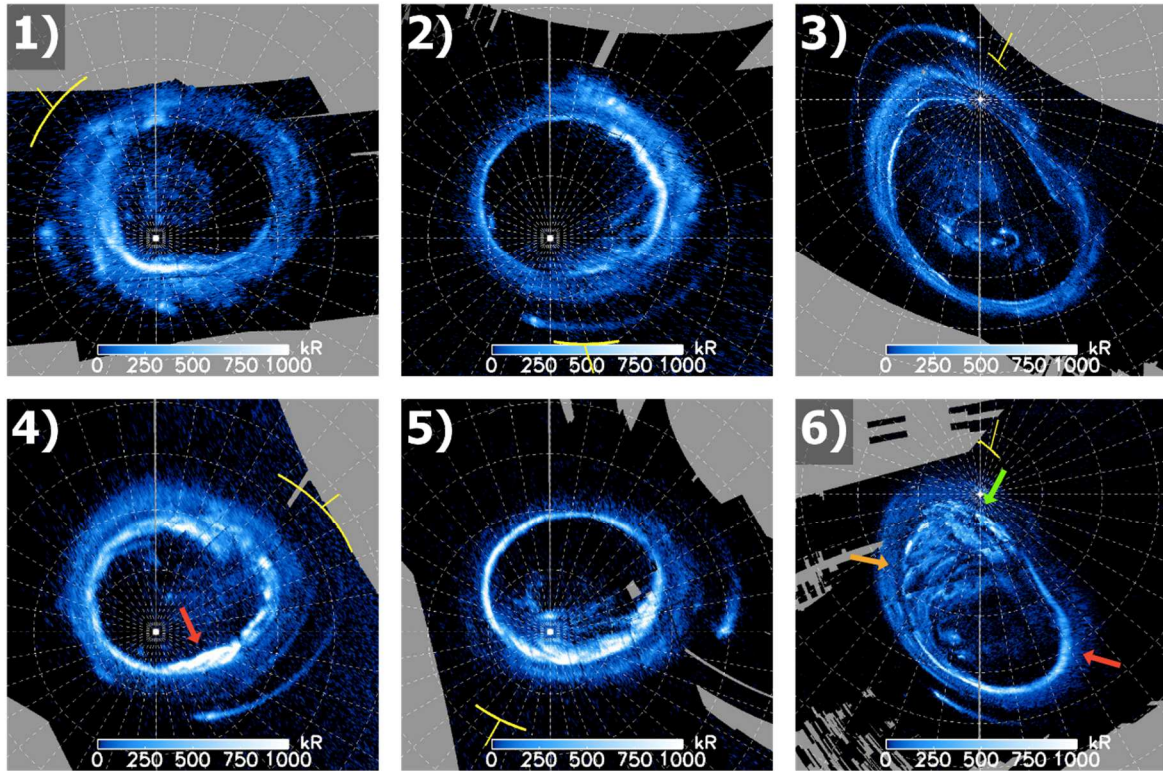
423



424

425 Figure 2: Top: dusk-over-dawn power ratios for the different sectors as a function of subsolar
 426 longitude. Bottom: Zoomed version of the same plot, centered on the value 1. One can see that the
 427 different methods can provide different results for individual cases, but for every method, dusk-
 428 over-dawn ratios above 1 vastly outnumber those under 1.

429



430

431 Figure 3: Illustration of three typical cases where the dusk region is more powerful than the dawn
 432 one (top line) and three atypical cases where the dawn region is more powerful than the dusk one
 433 (bottom line). The yellow arc and tick mark show the orientation of the Sun during the image
 434 acquisition. 1) Polar projection of the southern pole during PJ5. 2) Polar projection of the southern
 435 pole during PJ7. 3) Polar projection of the northern pole during PJ13. 4) Polar projection of the
 436 southern pole during PJ32. A dawn storm is indicated by the red arrow. 5) Polar projection of the
 437 southern pole during PJ12. An enhancement of the main emissions at all longitudes is visible. 6)
 438 Polar projection of the northern pole during PJ26. The red arrow points toward the dawn part of the
 439 main emissions where they are clearly visible. The green arrow points toward the noon part, where
 440 they are harder to distinguish from the polar emissions but still recognizable. Finally, the orange
 441 arrow points toward the dusk region, where the main emissions vanished and a strong decrease in
 442 the brightness is visible between the polar and outer emissions. In the three images, the sunward
 443 direction is indicated the same way as in Figure 1.

444

		B15 sector Median	SYM sector Median
MD mask	North	3.40	3.04
	South	4.24	2.92
AF1 mask	North	3.43	2.94
	South	4.73	3.22
AF2 mask	North	3.91	3.25
	South	5.47	4.04

445

446 Table 1: Median dusk-over-dawn power ratios for the MD, AF1 and AF2 masks in the southern and
447 northern hemispheres, for both the B15 and SYM sectors.

448

449 **6| Acknowledgements**

450

451 We are grateful to NASA and contributing institutions which have made the Juno mission
452 possible. B. Bonfond is a Research Associate of the Fonds de la Recherche Scientifique -
453 FNRS. B. Bonfond, D. Grodent and J.-C. Gérard acknowledge financial support from the
454 Belgian Federal Science Policy Office (BELSPO) via the PRODEX Programme of ESA. This work
455 was funded by NASA's New Frontiers Program for Juno via contract with the Southwest
456 Research Institute. VH acknowledges support from the French government under the France
457 2030 investment plan, as part of the Initiative d'Excellence d'Aix-Marseille Université –
458 A*MIDEX AMX-22-CPJ-04.

459

460 **References**

461

462 Bolton, S.J., Lunine, J., Stevenson, D., Connerney, J.E.P., Levin, S., Owen, T.C., Bagenal, F.,
463 Gautier, D., Ingersoll, A.P., Orton, G.S., Guillot, T., Hubbard, W., Bloxham, J., Coradini, A.,
464 Stephens, S.K., Mokashi, P., Thorne, R., Thorpe, R., 2017. The Juno Mission. *Space Sci Rev*
465 213, 5–37. <https://doi.org/10.1007/s11214-017-0429-6>

466 Bonfond, B., Grodent, D., Gérard, J.-C., Stallard, T., Clarke, J.T., Yoneda, M., Radioti, A.,
467 Gustin, J., 2012. Auroral evidence of Io's control over the magnetosphere of Jupiter.
468 *Geophysical Research Letters* 39. <https://doi.org/10.1029/2011GL050253>

469 Bonfond, B., Gustin, J., Gérard, J.-C., Grodent, D., Radioti, A., Palmaerts, B., Badman, S.V.,
470 Khurana, K.K., Tao, C., 2015. The far-ultraviolet main auroral emission at Jupiter – Part 1:
471 Dawn–dusk brightness asymmetries. *Annales Geophysicae* 33, 1203–1209.
472 <https://doi.org/10.5194/angeo-33-1203-2015>

473 Bonfond, B., Yao, Z., Grodent, D., 2020. Six Pieces of Evidence Against the Corotation
474 Enforcement Theory to Explain the Main Aurora at Jupiter. *Journal of Geophysical Research:*
475 *Space Physics* 125, e2020JA028152. <https://doi.org/10.1029/2020JA028152>

476 Bonfond, B., Yao, Z.H., Gladstone, G.R., Grodent, D., Gérard, J.-C., Matar, J., Palmaerts, B.,
477 Greathouse, T.K., Hue, V., Versteeg, M.H., Kammer, J.A., Giles, R.S., Tao, C., Vogt, M.F.,
478 Mura, A., Adriani, A., Mauk, B.H., Kurth, W.S., Bolton, S.J., 2021. Are Dawn Storms Jupiter's
479 Auroral Substorms? *AGU Advances* 2, e2020AV000275.
480 <https://doi.org/10.1029/2020AV000275>

481 Clarke, J.T., Nichols, J., Gérard, J.-C., Grodent, D., Hansen, K.C., Kurth, W., Gladstone, G.R.,
482 Duval, J., Wannawichian, S., Bunce, E., Cowley, S.W.H., Cray, F., Dougherty, M., Lamy, L.,

483 Mitchell, D., Pryor, W., Retherford, K., Stallard, T., Zieger, B., Zarka, P., Cecconi, B., 2009.
484 Response of Jupiter's and Saturn's auroral activity to the solar wind. *Journal of Geophysical*
485 *Research: Space Physics* 114. <https://doi.org/10.1029/2008JA013694>

486 Connerney, J.E.P., Kotsiaros, S., Oliverson, R.J., Espley, J.R., Joergensen, J.L., Joergensen, P.S.,
487 Merayo, J.M.G., Herceg, M., Bloxham, J., Moore, K.M., Bolton, S.J., Levin, S.M., 2018. A New
488 Model of Jupiter's Magnetic Field From Juno's First Nine Orbits. *Geophysical Research*
489 *Letters* 45, 2590–2596. <https://doi.org/10.1002/2018GL077312>

490 Connerney, J.E.P., Timmins, S., Oliverson, R.J., Espley, J.R., Joergensen, J.L., Kotsiaros, S.,
491 Joergensen, P.S., Merayo, J.M.G., Herceg, M., Bloxham, J., Moore, K.M., Mura, A., Moirano,
492 A., Bolton, S.J., Levin, S.M., 2022. A New Model of Jupiter's Magnetic Field at the
493 Completion of Juno's Prime Mission. *Journal of Geophysical Research: Planets* 127,
494 e2021JE007055. <https://doi.org/10.1029/2021JE007055>

495 Cowley, S.W.H., Bunce, E.J., 2001. Origin of the main auroral oval in Jupiter's coupled
496 magnetosphere–ionosphere system. *Planetary and Space Science, Magnetosphere of the*
497 *Outer Planets Part II* 49, 1067–1088. [https://doi.org/10.1016/S0032-0633\(00\)00167-7](https://doi.org/10.1016/S0032-0633(00)00167-7)

498 Davis, M.W., Gladstone, G.R., Greathouse, T.K., Slater, D.C., Versteeg, M.H., Persson, K.B.,
499 Winters, G.S., Persyn, S.C., Eterno, J.S., 2011. Radiometric performance results of the Juno
500 ultraviolet spectrograph (Juno-UVS), in: *UV/Optical/IR Space Telescopes and Instruments:*
501 *Innovative Technologies and Concepts V. Presented at the UV/Optical/IR Space Telescopes*
502 *and Instruments: Innovative Technologies and Concepts V, SPIE*, pp. 42–54.
503 <https://doi.org/10.1117/12.894274>

504 Feng, E., Zhang, B., Yao, Z., Delamere, P.A., Zheng, Z., Brambles, O.J., Ye, S.-Y., Sorathia, K.A.,
505 2022. Dynamic Jovian Magnetosphere Responses to Enhanced Solar Wind Ram Pressure:
506 Implications for Auroral Activities. *Geophysical Research Letters* 49, e2022GL099858.
507 <https://doi.org/10.1029/2022GL099858>

508 Gérard, J.-C., Bonfond, B., Grodent, D., Radioti, A., 2016. The color ratio-intensity relation in
509 the Jovian aurora: Hubble observations of auroral components. *Planetary and Space Science*
510 131, 14–23. <https://doi.org/10.1016/j.pss.2016.06.004>

511 Gladstone, G.R., Persyn, S.C., Eterno, J.S., Walther, B.C., Slater, D.C., Davis, M.W., Versteeg,
512 M.H., Persson, K.B., Young, M.K., Dirks, G.J., Sawka, A.O., Tumlinson, J., Sykes, H., Beshears,
513 J., Rhoad, C.L., Cravens, J.P., Winters, G.S., Klar, R.A., Lockhart, W., Piepgrass, B.M.,
514 Greathouse, T.K., Trantham, B.J., Wilcox, P.M., Jackson, M.W., Siegmund, O.H.W., Vallergera,
515 J.V., Raffanti, R., Martin, A., Gérard, J.-C., Grodent, D.C., Bonfond, B., Marquet, B., Denis, F.,
516 2017. The Ultraviolet Spectrograph on NASA's Juno Mission. *Space Sci Rev* 213, 447–473.
517 <https://doi.org/10.1007/s11214-014-0040-z>

518 Grodent, D., 2015. A Brief Review of Ultraviolet Auroral Emissions on Giant Planets. *Space*
519 *Sci Rev* 187, 23–50. <https://doi.org/10.1007/s11214-014-0052-8>

520 Grodent, D., Bonfond, B., Gérard, J.-C., Radioti, A., Gustin, J., Clarke, J.T., Nichols, J.,
521 Connerney, J.E.P., 2008. Auroral evidence of a localized magnetic anomaly in Jupiter's

522 northern hemisphere. *Journal of Geophysical Research: Space Physics* 113.
523 <https://doi.org/10.1029/2008JA013185>

524 Grodent, D., Bonfond, B., Yao, Z., Gérard, J.-C., Radioti, A., Dumont, M., Palmaerts, B.,
525 Adriani, A., Badman, S.V., Bunce, E.J., Clarke, J.T., Connerney, J.E.P., Gladstone, G.R.,
526 Greathouse, T., Kimura, T., Kurth, W.S., Mauk, B.H., McComas, D.J., Nichols, J.D., Orton, G.S.,
527 Roth, L., Saur, J., Valek, P., 2018. Jupiter's Aurora Observed With HST During Juno Orbits 3 to
528 7. *Journal of Geophysical Research: Space Physics* 123, 3299–3319.
529 <https://doi.org/10.1002/2017JA025046>

530 Gustin, J., Bonfond, B., Grodent, D., Gérard, J.-C., 2012. Conversion from HST ACS and STIS
531 auroral counts into brightness, precipitated power, and radiated power for H2 giant planets.
532 *Journal of Geophysical Research: Space Physics* 117. <https://doi.org/10.1029/2012JA017607>

533 Hill, T.W., 2001. The Jovian auroral oval. *J. Geophys. Res.* 106, 8101–8108.
534 <https://doi.org/10.1029/2000JA000302>

535 Hue, V., Giles, R.S., Gladstone, G.R., Greathouse, T.K., Davis, M.W., Kammer, J.A., Versteeg,
536 M.H., 2021. Updated radiometric and wavelength calibration of the Juno ultraviolet
537 spectrograph. *Journal of Astronomical Telescopes, Instruments, and Systems* 7, 044003.
538 <https://doi.org/10.1117/1.JATIS.7.4.044003>

539 Hue, V., Gladstone, G.R., Greathouse, T.K., Kammer, J.A., Davis, M.W., Bonfond, B.,
540 Versteeg, M.H., Grodent, D.C., Gérard, J.-C., Bolton, S.J., Levin, S.M., Byron, B.D., 2019. In-
541 flight Characterization and Calibration of the Juno-ultraviolet Spectrograph (Juno-UVS). *The*
542 *Astronomical Journal* 157, 90. <https://doi.org/10.3847/1538-3881/aafb36>

543 Kamran, A., Bunce, E.J., Cowley, S.W.H., James, M.K., Nichols, J.D., Provan, G., Cao, H., Hue,
544 V., Greathouse, T.K., Gladstone, G.R., 2022. Auroral Field-Aligned Current Signatures in
545 Jupiter's Magnetosphere: Juno Magnetic Field Observations and Physical Modeling. *Journal*
546 *of Geophysical Research: Space Physics* 127, e2022JA030431.
547 <https://doi.org/10.1029/2022JA030431>

548 Khurana, K.K., 2001. Influence of solar wind on Jupiter's magnetosphere deduced from
549 currents in the equatorial plane. *Journal of Geophysical Research: Space Physics* 106,
550 25999–26016. <https://doi.org/10.1029/2000JA000352>

551 Kotsiaros, S., Connerney, J.E.P., Clark, G., Allegrini, F., Gladstone, G.R., Kurth, W.S., Mauk,
552 B.H., Saur, J., Bunce, E.J., Gershman, D.J., Martos, Y.M., Greathouse, T.K., Bolton, S.J., Levin,
553 S.M., 2019. Birkeland currents in Jupiter's magnetosphere observed by the polar-orbiting
554 Juno spacecraft. *Nat Astron* 3, 904–909. <https://doi.org/10.1038/s41550-019-0819-7>

555 Lorch, C.T.S., Ray, L.C., Arridge, C.S., Khurana, K.K., Martin, C.J., Bader, A., 2020. Local Time
556 Asymmetries in Jupiter's Magnetodisc Currents. *Journal of Geophysical Research: Space*
557 *Physics* 125, e2019JA027455. <https://doi.org/10.1029/2019JA027455>

558 Lorch, C.T.S., Ray, L.C., Wilson, R.J., Bagenal, F., Cray, F., Delamere, P.A., Damiano, P.A.,
559 Watt, C.E.J., Allegrini, F., 2022. Evidence of Alfvénic Activity in Jupiter's Mid-To-High Latitude

560 Magnetosphere. *Journal of Geophysical Research: Space Physics* 127, e2021JA029853.
561 <https://doi.org/10.1029/2021JA029853>

562 Nichols, J.D., Badman, S.V., Bagenal, F., Bolton, S.J., Bonfond, B., Bunce, E.J., Clarke, J.T.,
563 Connerney, J.E.P., Cowley, S.W.H., Ebert, R.W., Fujimoto, M., Gérard, J.-C., Gladstone, G.R.,
564 Grodent, D., Kimura, T., Kurth, W.S., Mauk, B.H., Murakami, G., McComas, D.J., Orton, G.S.,
565 Radioti, A., Stallard, T.S., Tao, C., Valek, P.W., Wilson, R.J., Yamazaki, A., Yoshikawa, I.,
566 2017a. Response of Jupiter's auroras to conditions in the interplanetary medium as
567 measured by the Hubble Space Telescope and Juno. *Geophysical Research Letters* 44, 7643–
568 7652. <https://doi.org/10.1002/2017GL073029>

569 Nichols, J.D., Bunce, E.J., Clarke, J.T., Cowley, S.W.H., Gérard, J.-C., Grodent, D., Pryor, W.R.,
570 2007. Response of Jupiter's UV auroras to interplanetary conditions as observed by the
571 Hubble Space Telescope during the Cassini flyby campaign. *Journal of Geophysical Research:*
572 *Space Physics* 112. <https://doi.org/10.1029/2006JA012005>

573 Nichols, J.D., Clarke, J.T., Gérard, J.C., Grodent, D., Hansen, K.C., 2009. Variation of different
574 components of Jupiter's auroral emission. *Journal of Geophysical Research: Space Physics*
575 114. <https://doi.org/10.1029/2009JA014051>

576 Nichols, J.D., Cowley, S.W.H., 2022. Relation of Jupiter's Dawnside Main Emission Intensity
577 to Magnetospheric Currents During the Juno Mission. *Journal of Geophysical Research:*
578 *Space Physics* 127, e2021JA030040. <https://doi.org/10.1029/2021JA030040>

579 Nichols, J.D., Yeoman, T.K., Bunce, E.J., Chowdhury, M.N., Cowley, S.W.H., Robinson, T.R.,
580 2017b. Periodic Emission Within Jupiter's Main Auroral Oval. *Geophysical Research Letters*
581 44, 9192–9198. <https://doi.org/10.1002/2017GL074824>

582 Pan, D.-X., Yao, Z.-H., Manners, H., Dunn, W., Bonfond, B., Grodent, D., Zhang, B.-Z., Guo, R.-
583 L., Wei, Y., 2021. Ultralow-Frequency Waves in Driving Jovian Aurorae Revealed by
584 Observations From HST and Juno. *Geophysical Research Letters* 48, e2020GL091579.
585 <https://doi.org/10.1029/2020GL091579>

586 Radioti, A., Gérard, J.-C., Grodent, D., Bonfond, B., Krupp, N., Woch, J., 2008. Discontinuity in
587 Jupiter's main auroral oval. *Journal of Geophysical Research: Space Physics* 113.
588 <https://doi.org/10.1029/2007JA012610>

589 Ray, L.C., Achilleos, N.A., Vogt, M.F., Yates, J.N., 2014. Local time variations in Jupiter's
590 magnetosphere-ionosphere coupling system. *Journal of Geophysical Research: Space*
591 *Physics* 119, 4740–4751. <https://doi.org/10.1002/2014JA019941>

592 Saur, J., Janser, S., Schreiner, A., Clark, G., Mauk, B.H., Kollmann, P., Ebert, R.W., Allegrini, F.,
593 Szalay, J.R., Kotsiaros, S., 2018. Wave-Particle Interaction of Alfvén Waves in Jupiter's
594 Magnetosphere: Auroral and Magnetospheric Particle Acceleration. *Journal of Geophysical*
595 *Research: Space Physics* 123, 9560–9573. <https://doi.org/10.1029/2018JA025948>

596 Sulaiman, A.H., Mauk, B.H., Szalay, J.R., Allegrini, F., Clark, G., Gladstone, G.R., Kotsiaros, S.,
597 Kurth, W.S., Bagenal, F., Bonfond, B., Connerney, J.E.P., Ebert, R.W., Elliott, S.S., Gershman,
598 D.J., Hospodarsky, G.B., Hue, V., Lysak, R.L., Masters, A., Santolík, O., Saur, J., Bolton, S.J.,

599 2022. Jupiter's Low-Altitude Auroral Zones: Fields, Particles, Plasma Waves, and Density
600 Depletions. *Journal of Geophysical Research: Space Physics* 127, e2022JA030334.
601 <https://doi.org/10.1029/2022JA030334>

602 Tao, C., Sahraoui, F., Fontaine, D., de Patoul, J., Chust, T., Kasahara, S., Retinò, A., 2015.
603 Properties of Jupiter's magnetospheric turbulence observed by the Galileo spacecraft.
604 *Journal of Geophysical Research: Space Physics* 120, 2477–2493.
605 <https://doi.org/10.1002/2014JA020749>

606 Vogt, M.F., Kivelson, M.G., Khurana, K.K., Walker, R.J., Bonfond, B., Grodent, D., Radioti, A.,
607 2011. Improved mapping of Jupiter's auroral features to magnetospheric sources. *Journal of*
608 *Geophysical Research: Space Physics* 116. <https://doi.org/10.1029/2010JA016148>

609 Yao, Z.H., Bonfond, B., Grodent, D., Chané, E., Dunn, W.R., Kurth, W.S., Connerney, J.E.P.,
610 Nichols, J.D., Palmaerts, B., Guo, R.L., Hospodarsky, G.B., Mauk, B.H., Kimura, T., Bolton, S.J.,
611 2022. On the Relation Between Auroral Morphologies and Compression Conditions of
612 Jupiter's Magnetopause: Observations From Juno and the Hubble Space Telescope. *Journal*
613 *of Geophysical Research: Space Physics* 127, e2021JA029894.
614 <https://doi.org/10.1029/2021JA029894>

615 Yung, Y.L., Gladstone, G.R., Chang, K.M., Ajello, J.M., Srivastava, S.K., 1982. H₂ fluorescence
616 spectrum from 1200 to 1700 Å by electron impact - Laboratory study and application to
617 Jovian aurora. *The Astrophysical Journal* 254, L65–L69. <https://doi.org/10.1086/183757>

618

619